Solution structure, dynamics and tetrahedral assembly of Anti-TRAP, a homo-trimeric triskelion-shaped regulator of tryptophan biosynthesis in *Bacillus subtilis*

Craig McElroy[1,2], Elihu Ihms[2,3], Deepak Kumar Yadav[2], Melody Holmquist,[1,2] Vibhuti Wadwha[2], Vicki Wysocki[2,5], Paul Gollnick[4], and Mark Foster[1,2,3]*

[1] Ohio State Biochemistry Program

[2] Department of Chemistry and Biochemistry, The Ohio State University, Columbus, OH 43210

[3] Biophysics Program

[4] Department of Biological Sciences, State University of New York, Buffalo NY 14260

[5] National Resource for Native MS-Guided Structural Biology

*Corresponding author contact information:

Phone: 614-292-1377

Email: foster.281@osu.edu

Abstract

Cellular production of tryptophan is metabolically expensive and tightly regulated. The small *Bacillus subtilis* zinc binding Anti-TRAP protein (AT), which is the product of the *yczA/rtpA* gene, is upregulated in response to accumulating levels of uncharged $tRNA^{Trp}$ through a T-box antitermination mechanism. AT binds to the undecameric ring-shaped protein TRAP (*trp* RNA Binding Attenuation Protein), thereby preventing it from binding to the *trp* leader RNA. This reverses the inhibitory effect of TRAP on transcription and translation of the *trp* operon. AT principally adopts two symmetric oligomeric states, a trimer (AT_3) featuring a three-helix bundle, or a dodecamer (AT_{12}) comprising a tetrahedral assembly of trimers, whereas only the trimeric form has been shown to bind and inhibit TRAP. We demonstrate the utility of native mass spectrometry (nMS) and small-angle x-ray scattering (SAXS), together with analytical ultracentrifugation (AUC) for monitoring the pH and concentration-dependent equilibrium between the trimeric and dodecameric structural forms of AT. In addition, we report the use of solution nuclear magnetic resonance (NMR) spectroscopy to determine the solution structure of AT_3, while heteronuclear ^{15}N relaxation measurements on both oligomeric forms of AT provide insights into the dynamic properties of binding-active AT_3 and binding-inactive AT_{12}, with implications for TRAP inhibition.

Introduction

The *trp* RNA-binding attenuation protein (TRAP) senses intracellular levels of tryptophan in order to regulate transcription [1–4] and translation [5–10] of the genes required for tryptophan biosynthesis (Figure 1). Transcriptional and translational control by TRAP depends on the ability of tryptophan-bound TRAP to bind to an RNA site with multiple (G/U)AG repeats separated by two or three nonconserved spacer nucleotides [1]. The transcription of the six tryptophan biosynthetic genes clustered in the *trpECDFBA* operon [11] is controlled through an attenuation mechanism by which TRAP binding is thought to remodel competing secondary structural elements in the 5′ leader region of the nascent mRNA: in the absence of tryptophan, RNA binding by TRAP is impaired, and the leader folds into an anti-terminator hairpin that allows transcription of the entire operon. Increased cellular tryptophan binds to TRAP, activating it to bind to its RNA target which overlaps with and prevents formation of the anti-terminator hairpin; instead, a small downstream terminator hairpin forms and transcription of the structural genes is attenuated [2]. There is considerable evidence in support of this terminator/anti-terminator model, although TRAP nevertheless induces attenuation in the absence of an intact terminator [12,13].

Translational control of *trpE* [9,14], and perhaps the entire *trp* operon, is also accomplished through TRAP binding-dependent RNA secondary structure [8]. When TRAP is inactive and cannot bind to the read-through transcript of the *trp* operon, the Shine-Dalgarno (SD) sequence of the *trpE* gene is unstructured and allows ribosome binding. When Trp-activated TRAP binds to the untranslated region of the transcript, the *trpE* SD sequence becomes sequestered in a hairpin that forms downstream of the TRAP binding site, thereby preventing ribosome binding and translation initiation [9]. TRAP binding sites are also present in the transcripts of the *trpG*,

trpP, and *ycbK* genes, but in the translation initiation region, where TRAP binding directly impedes ribosome binding and thereby regulates translation [1,6,15,16].
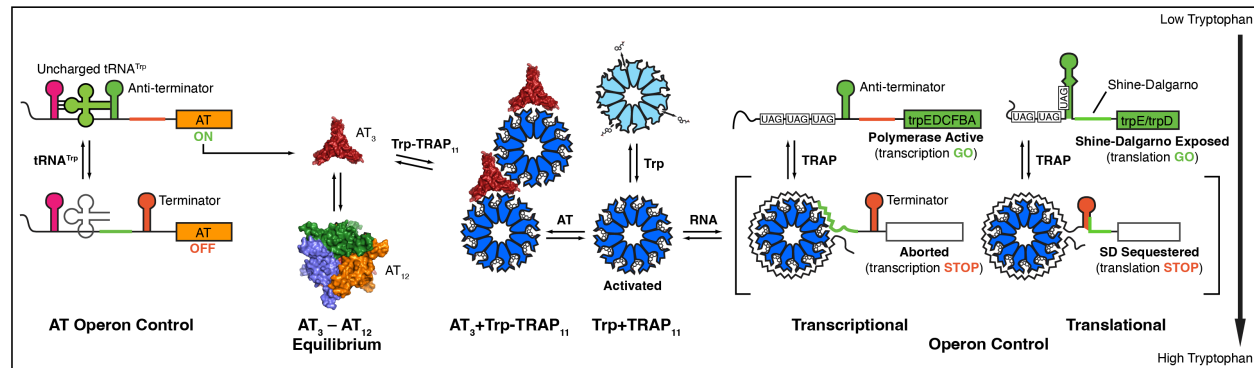

Figure 1. Transcription and translation of the *trp* operon in *B. subtilis* is regulated by feedback loops involving the functions of two proteins: the ring-shaped 11-mer TRAP, which senses free Trp, and Anti-TRAP (AT) which is overexpressed in response to accumulation of uncharged tRNA^{Trp}. In the absence of AT, Trp-bound TRAP (blue) binds a series of UAG and GAG triplets in the 5' leader of the *trp* operon, resulting in transcriptional and translational repression in part by formation of a terminator or sequestering the Shine-Dalgarno (SD) sequence. When expressed, trimeric AT (AT$_3$) can bind to Trp-activated TRAP, preventing RNA binding and blocking its inhibition of Trp biosynthesis. AT exists in equilibrium between trimeric (red) and dodecameric states (blue, orange, green; the red trimer is behind the other three), while only trimeric AT binds and inhibits TRAP.

In many bacteria, the extent of charging of tRNA^{Trp} is sensed as a regulatory signal in addition to the levels of free tryptophan [17,18]. In studies with a temperature-sensitive mutant of the tryptophanyl-tRNA synthetase in *B. subtilis*, the accumulation of uncharged tRNA^{Trp} leads to over-expression of the *trpECDFBA* operon [15]. The operon responsible for this effect was shown to be regulated via the T-box transcription anti-termination mechanism, where uncharged tRNA^{Trp} specifically pairs with the leader RNA causing anti-termination and transcriptional read-through [6]. Deletions within the operon identified *yczA/rtpA* as the responsible gene, and the protein product, anti-TRAP (AT), was shown to inhibit TRAP activity [6,19,20]. Expression of AT was also shown to be regulated at the level of translation by tRNA-dependent ribosome stalling [21,22].
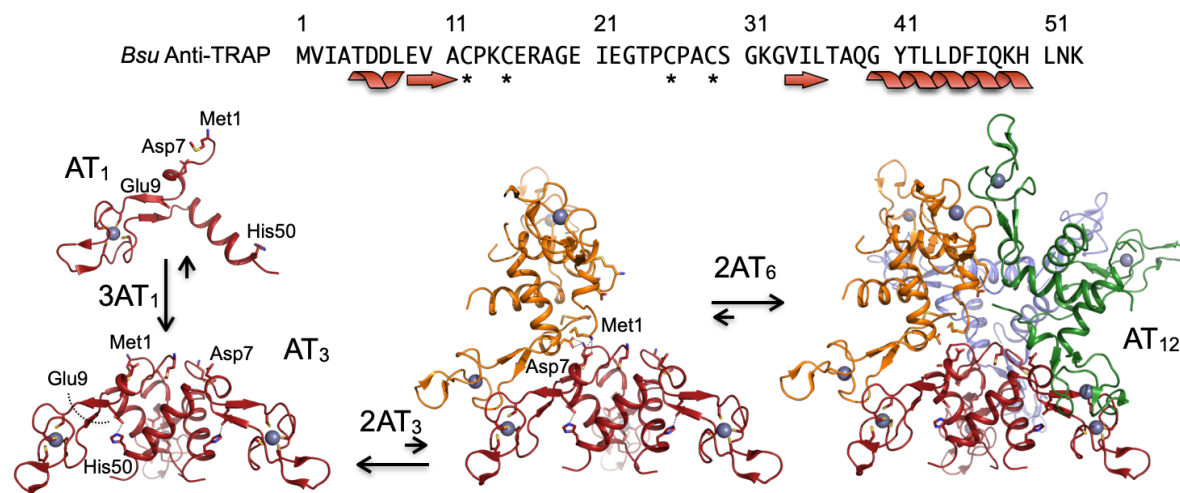
Figure 2. Oligomeric assembly of *Bsu* Anti-TRAP (AT). The 53-residue AT protomer (AT$_1$) features a short N-terminal helix leading into a "zinc ribbon" motif and ending in a C-terminal helix. Assembly of AT$_3$ occurs via a helical bundle that buries ~4,200 Å². In solution AT$_3$ is in an equilibrium with dodecamers (AT$_{12}$) featuring a tetrahedral arrangement of AT$_3$ stabilized by a network of ion pairs between the amino terminus of Met1 and the sidechain carboxylate of Asp7 of adjacent trimers. A transient AT$_6$ intermediate is hypothesized to arise from dimerization of AT$_3$ via formation of two sets of Met1-Asp7 ion pairs and burial of ~1,100 Å²; dimerization of two AT$_6$ assemblies to form AT$_{12}$ is favored by formation of ten additional sets of ion pairs and burial of another ~4,600 Å².

Symmetry mismatch between the oligomeric states of AT and TRAP was evident from early chemical cross-linking, analytical ultracentrifugation, native mass spectrometry and NMR studies [19,23–26]. Diffracting crystals of *Bsu* AT revealed a dodecamer (AT$_{12}$) arranged as a tetrahedral tetramer of trimers (AT$_3$)$_4$ (Figure 2) [27–29]. Each AT protomer forms a short helix (residues 5-8) at the N-terminus, β-strands from residues 9-11 and 34-36 form a short anti-parallel β-sheet; a β-hairpin is formed by strands from residues 20-21 and 24-25, and an α-helix is present at the C-terminus from residues 38-50. Trimers are arranged via a three-helix bundle involving the C-terminal helix, with the zinc binding domains extended outward from the C$_3$ helical axis. The AT dodecamer is formed through complementary inter-trimer ion pair interactions involving an N-terminal amine and a sidechain carboxylate from each trimer, as well as hydrophobic surface burial of the zinc-binding regions (Figure 2) [27–29]. Because the stabilizing ion pair requires a protonated N-terminus, which has a pKa near pH 7 [30], assembly

of the dodecamer is disfavored above pH ~8 [26]. The *B. licheniformis* variant of AT (which shares a 76% sequence identity with *B. subtilis* AT) crystallized at low pH adopts the same dodecameric structure as the *Bsu* protein, but at high pH the trimers assemble in an inverted orientation, with their N-termini projecting into solvent [29].

AT binds asymmetrically to Trp-loaded TRAP. Although *Bsu* TRAP is predominantly undecameric, both undecamers and dodecamers are observed in mass spectra [1,31–33], and crystallographic studies of *Bsu* AT bound to dodecameric TRAP rings revealed AT_3 docked on the RNA binding surface of $TRAP_{12}$, via protein-protein surfaces of the zinc binding and helical domains that are not accessible in AT_{12} [34]. Mass spectrometric, solution small angle scattering, and analytical ultracentrifugation experiments [35] are also consistent with a model in which only AT_3 can compete with RNA for the TRAP-RNA binding site. These findings suggest that the $AT_3 \leftrightarrow AT_{12}$ equilibrium may represent an additional regulatory step.

We found experimentally that preventing formation of the inter-trimer Met1-Asp7 ion pairs favors AT_3, even at high protein concentrations [26]. Addition of excess zinc during protein recombinant production of AT in *E. coli* results in significant accumulation of formylmethionine AT (*f*AT), presumably due to poisoning of peptide deformylase [36,37]; the resulting immature *f*AT can be chromatographically separated from mature AT under denaturing conditions [26]. Other modification to the N-terminus, such as inclusion of a His-6 tag, similarly prevents AT_{12} formation [38]. This provides the means to experimentally produce homogenous samples of either AT_3 or AT_{12}, to allow characterization of the two oligomers in the absence of confounding effects from their equilibrium.

We have leveraged the ability to selectively produce AT trimers and dodecamers to determine the solution structure of *Bsu* AT_3 and to examine the pH- and concentration-dependent equilibrium between to AT_3 and AT_{12} using small angle x-ray scattering (SAXS), sedimentation velocity analytical ultracentrifugation (AUC), and native mass spectrometry (nMS). In addition, backbone amide ^{15}N NMR relaxation measurements [39–41] allowed us to study the dynamics of both the trimeric and dodecameric AT forms. These results provide new insights into the structural basis of Anti-TRAP's homo-oligomeric assembly, and how this process may modulate AT's function in its regulatory context.

Results

Anti-TRAP (AT) adopts trimeric and dodecameric species in solution

NMR and native MS reveal two states in slow equilibrium

At pH values near 7, purified AT samples at 10^{-3} M concentrations yield ^{15}N HSQC spectra that exhibit doubling of many amide resonances; such doubling arises in cases of chemical heterogeneity or slow conformational exchange between two states. After chromatographically separating
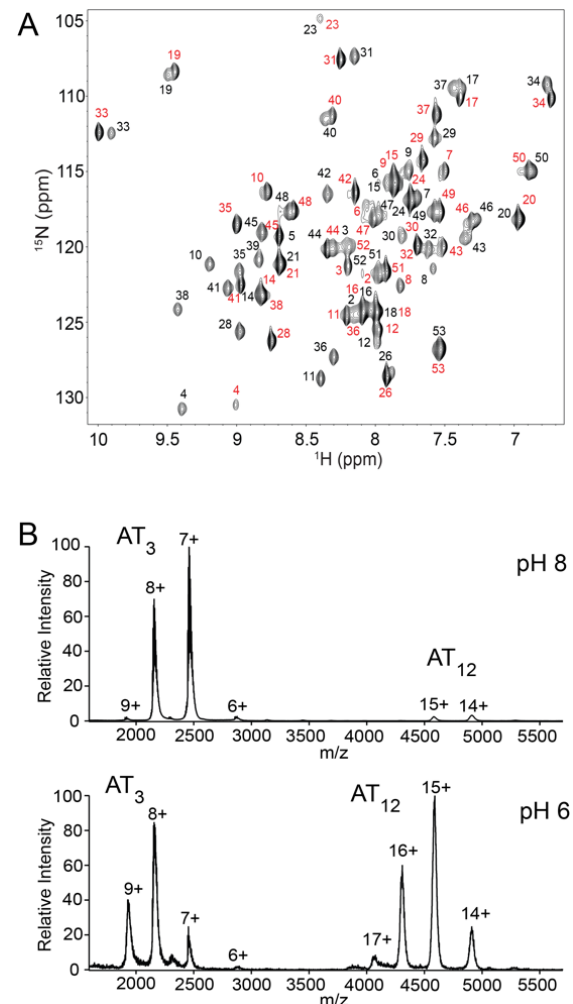

Figure 3. AT adopts trimeric and dodecameric states in solution. (A) ^{15}N-^1H NMR spectrum of 1 mM AT, pH 7.5 reveals doubling of many signals; residue assignments as indicated (black, AT_3; red, AT_{12}). (B) Native MS in 100 mM AmAc shows trimers are favored at pH 8 and 12-mers are favored at pH 6; predicted (Zn-AT)$_3$: 17,144.9 Da; (Zn-AT)$_{12}$: 68,579.4 Da; observed at pH 6: 17,181.8 ± 63.7 Da and 68,826.5 ± 76.4 Da; observed at pH 8: 17,181.5 ± 55.3 Da and 68,751.5 ± 47.3 Da. Other oligomeric states are not evident. The extra mass can be attributed to salt and/or solvent adducts, typical for the instrument used.

mature AT from immature formylated AT (fAT) under denaturing conditions [26], samples of mature AT produced the same signal doubling (Figure 3), indicating that it is not due to chemical heterogeneity. Nano electrospray ionization mass spectrometry under soft ionization conditions, at protein concentrations one hundred times lower than NMR (10^{-5} M), yielded two sets of ions, one corresponding to the mass of AT_3, and the other, AT_{12} (Figure 3). Adjusting the solution pH to 8 produced a higher proportion of AT_3 ions, while at pH 6 similar intensities were observed for both sets of ions, consistent with prior findings from pH-dependent NMR spectra. In addition to affecting the oligomeric state, changing the pH slightly altered the preferred charge state distribution: at pH 8, the 7+ and 14+ charge states were favored for AT_3 and AT_{12}, respectively; at pH 6, the 8+ and 15+ charge states dominate the spectrum. Although AT_3 and AT_{12} populations varied with pH, no other oligomeric species (e.g., AT_1, AT_6) were observed in the nMS data over a wide range of conditions.

Sedimentation velocity experiments provide evidence for a lowly populated hexamer intermediate

Guided by prior sedimentation velocity experiments at a fixed pH that revealed both AT_3 and AT_{12} in solution [23], we performed analytical ultracentrifugation sedimentation velocity experiments at pH 7, 7.25, 7.5, and 8 and a range of AT concentrations (Figure 4). For systems with components undergoing rapid exchange on the timescale of the sedimentation experiment, the modeling of boundary phases can provide the sedimentation coefficients for the components as well as the stepwise binding rates [42]. Sedimentation velocity data at each pH was globally fit across three concentrations in the program SEDPHAT [43], initially to a simple two-state model comprising the two states observed in NMR and MS spectra,

$$4AT_3 \underset{k_r}{\overset{k_f}{\rightleftharpoons}} AT_{12}$$
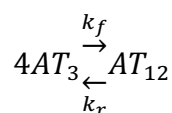
The resulting fits were poor, especially at alkaline conditions, and were better fit with a three-state exchange model,

$$4AT_3 \underset{k_{-1}}{\overset{k_1}{\rightleftharpoons}} 2AT_6 \underset{k_{-2}}{\overset{k_2}{\rightleftharpoons}} AT_{12}$$
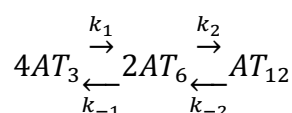
Lamm modeling of the sedimentation data predicts species with an intermediate sedimentation coefficient, which we attribute to a small population of hexamer AT_6, despite not observing this species by nMS or NMR (Figure 3). Fits to experimental interference fringe shifts using this model permitted optimization of two sets of apparent rate constants describing dimerization of AT_3 trimers into AT_6, and a subsequent dimerization of two AT_6 into AT_{12}. From the ratio of the fitted rate constants, we obtained consistent equilibrium dissociation constants for the first step, ranging from 20-90 μM over the experimental pH range. For the second
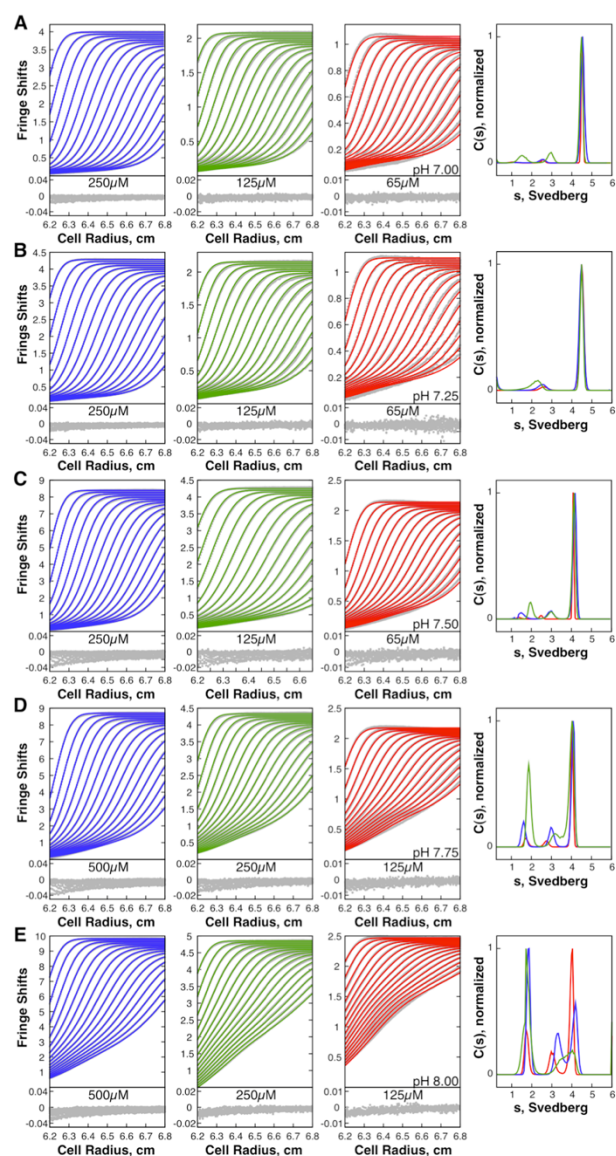

Figure 4. Sedimentation velocity experiments over a range of pH values can be fit with a three-state association model $AT_3 \leftrightarrow (AT_3)_2 \leftrightarrow AT_{12}$. Interference fringe shifts (gray dots) are globally fit across three AT concentrations (first three columns). Fits provided by the mechanistic model are in blue, green, and red lines. Only every tenth scan is shown. Residuals are below the data. Fourth column, sedimentation coefficient distributions with blue, red and green corresponding to the concentrations on the left, at pH 7.00 (A), pH 7.25 (B), pH 7.50 (C), pH 7.75 (D), and pH 8.00 (E).

step, the association rate constant dropped over three orders of magnitude over the same pH range, resulting in equilibrium constants from 0.05-50 µM. Thus, at low pH the second step is highly favored compared to the first step, resulting in very low concentrations of the hexameric intermediate AT_6. This is generally consistent with the relatively low populations of intermediate species in the fitted c(s) distributions (Figure 4). The excellent agreement between experimental and modeled data suggests that monomeric AT is not present at a significant population.

SAXS profiles of AT can be reconstructed from those of AT_3 and AT_{12} oligomers

We investigated the pH-dependent structure of AT using small angle x-ray scattering (SAXS). For mixtures, the resulting scattering profiles are the weighted sum of scattering profiles of the individual components [44]. Experimental scattering curves were de-convoluted using form factors for trimeric and dodecameric AT (Figure 5). The predicted scattering profiles for AT_3 and AT_{12} were calculated with CRYSOL [45] from the trimer and dodecamer assemblies in the crystal structure (2BX9) [28]. Deconvolution of the experimental data from the polydisperse AT solutions was performed using OLIGOMER [44]. The resulting fits using these two components describe the experimental data well, with AT_{12}
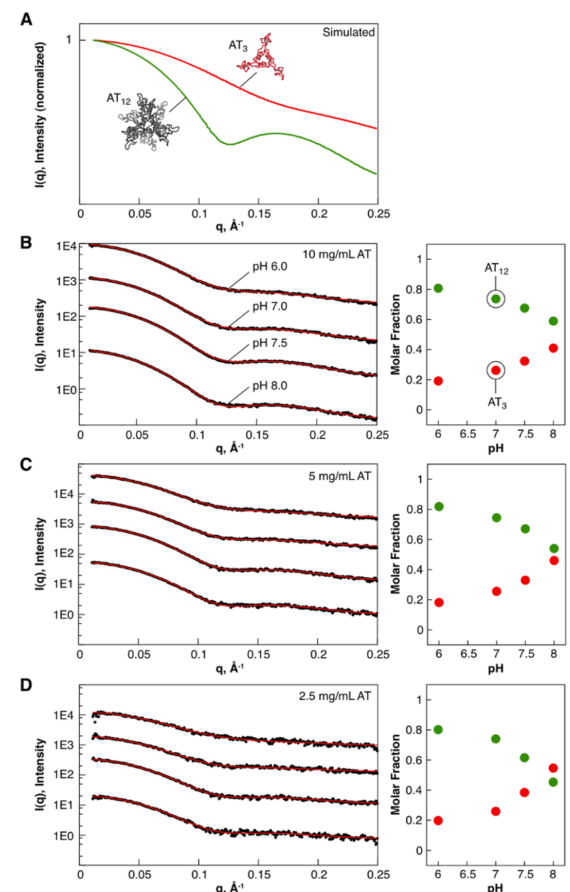

Figure 5. SAXS profiles of AT can be described as mixtures of AT_3 and AT_{12}. A, scattering curves for AT_3 and AT_{12}, computed from the dodecameric crystal structure (2bx9). B-D, left, experimental scattering intensities (black) for AT recorded over a range of pHs (6, 7, 7.5, 8) and concentrations (1.77, 0.89 and 0.44 mM), fit to a two-state model with varying fractions of AT_3 and AT_{12}. Profiles are offset in the y-axis from each other for visibility. Right, fitted volume fractions as a function of pH for each sampled concentration.

dominating below pH 7.5. We also tested for the presence of an inverted dodecameric structure such as that observed in crystallographic studies of *B. lichenformis* AT (PDB 3ld0) [29] by including its form factors in fitting the experimental data; this component was found to have zero weight in all of the tested experimental conditions. These data are consistent with a slow exchange between AT_3 and AT_{12} under near-physiological conditions, and a negligible population of intermediates.

NMR studies of *f*AT$_3$

Formylated AT is trimeric with high quality NMR spectra

We used immature *f*AT for detailed investigation of the structure and dynamics of the trimeric TRAP-binding oligomeric form. Since an ion pair between the protonated amine of Met1 and the sidechain carboxylate of Asp7 is proposed to stabilize the dodecameric structure [26,28], the formyl group prevents formation of the ion pair and *f*AT trimers do not oligomerize to form detectable dodecamers, even at millimolar concentrations at low pH. Resonance assignments and NMR
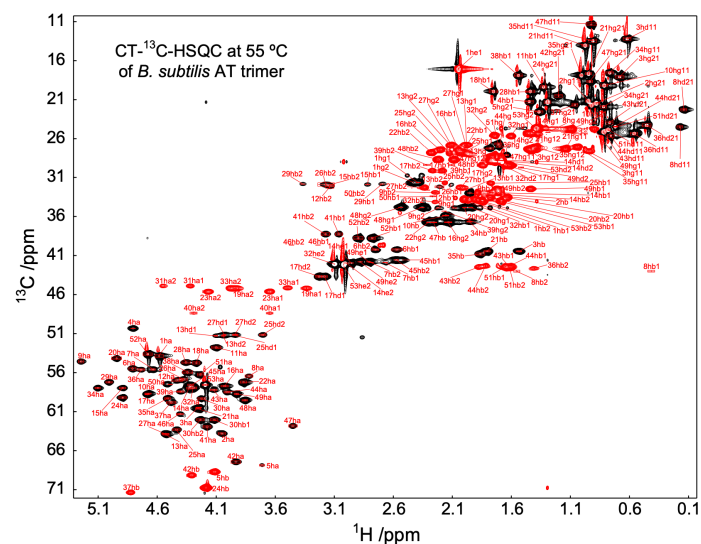

Figure 6. Symmetry and exceptional NMR spectra of *f*AT$_3$ allowed nearly complete resonance assignments. Aliphatic region of a two-dimensional constant-time ^{1}H-^{13}C correlation spectrum of *f*AT$_3$. In this spectrum ^{13}C resonances coupled to even (red) and odd (black) numbers of aliphatic carbons have opposite sign. Aliphatic carbon resonance assignments as indicated.

structural data were recorded at 55 °C, to match the conditions used for backbone resonance assignments of *Bst* TRAP [26,46,47].

NMR spectra of fAT$_3$ are of exceptionally high quality (e.g., Figure 6), enabling nearly complete backbone and side chain resonance assignments. *Bsu* AT comprises 53 amino acids, and zinc-bound fAT$_3$ has a nominal molecular mass of 17.1 kDa. Three-fold symmetry and fast tumbling result in narrow NMR resonances and high-quality heteronuclear correlation spectra. Backbone resonances were assigned from standard triple resonance spectra, while sidechain assignments were obtained from a combination of 2D and 3D double- and triple-resonance spectra. This allowed for assignment of every proton in the protein except for the side chain amine and hydroxyl protons.

The structure of fAT₃ is unperturbed by pH

SAXS, nMS and NMR data demonstrate that the trimer-dodecamer equilibrium is strongly affected by pH (Figure 3, Figure 4, Figure 5). This behavior was attributed to a near-neutral pKa for the amine at the N-terminus of the protein [30], and its ion pair with the

Figure 7. Protonation of the Met1 amine is coupled to oligomerization of AT. Left, ^{1}H-^{15}N correlated spectra of AT recorded at 25 °C and pH 6.5, 7.0, 7.5 and 8.0 reveal strong perturbations of several signals, and line narrowing at high pH, which favors trimeric AT. Right, for fAT the N-terminal amine is protected by the formyl group and very minor shift perturbations are observed only for residues flanking His50; this indicates no pH-dependent structural shifts in the AT trimer. Amide assignments transferred from 55 °C via a temperature series. (sc), side chain amide.

carboxylate side chain of Asp7 [26,28]. There is one other functional group in AT with a predicted pKa near neutrality: His50, which is conserved among AT variants [19,29]. In crystals the side chain imidazole Nε2 of His50, located at the end of the C-terminal helix, is observed to form an intra-chain ion pair with the carboxylate of Glu9, located in the zinc-ribbon motif (Figure 2). Changes in the protonation state of the imidazole side chain could conceivably alter
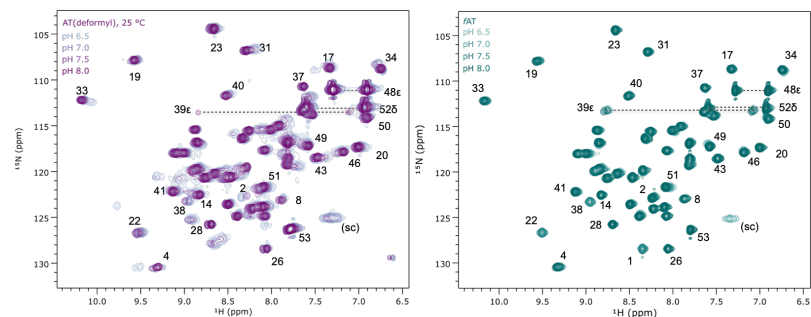
the geometry between the zinc-binding and helical domains and thus alter trimer packing in the dodecamer, driving changes in oligomeric structure (e.g., such behavior has been engineered into homo-oligomeric assemblies [48]). To examine whether His50 or another titratable group in the protein might induce structural changes that contribute to the pH-dependent oligomerization behavior, we recorded ^{1}H-^{15}N correlated NMR spectra of fAT over a range of pH values (Figure 7). Since fAT has a blocked N-terminus and does not form stable dodecamers, this allowed distinguishing spectral effects of ionization from those resulting from oligomerization. Correlation spectra of fAT recorded over a pH range that would shift the predominant oligomeric state from AT_3 to AT_{12} in the mature protein. result in only minor shifts in the spectra, particularly the amides of Lys49 and Leu51, reflecting their proximity to the His50 indole. This is consistent with a dominant role of a near neutral pKa for the N-terminal amide group in stabilizing the dodecamer.

Solution Structure Determination

The solution structure of the TRAP-binding oligomeric state of *Bsu* AT (AT_3) might be inferred from the 2.8 Å crystal structure of the dodecamer (2BX9)[28], the 2.1 Å structure of the *Bli* dodecamer (3LCZ)[29], and 3.2 Å structure of the *Bsu* AT bound to *Bst* TRAP (2ZP8) [34], but *de novo* structure determination was justified by the potential for perturbations from oligomerization and crystal packing. To that end, we determined the solution structure of fAT$_3$ using distance restraints from NOEs, orientation restraints from residual dipolar couplings, dihedral angle restraints from three-bond scalar couplings, three-fold symmetry restraints, and overall shape restraints from SAXS scattering curves.

Because of its homo-oligomeric structure and diverse source of restraints, structure determination proceeded via several steps. First, three-dimensional models of the zinc-bound AT protomer were computed from torsion angle restraints and NOEs that could be unambiguously assigned as being intramolecular. Next, we determined the solution structure of the trimer by replicating the chain and assigning as ambiguous all NOEs for which conservative distance filters prevented their assignment as being intramolecular. Most ambiguous NOEs could be assigned via iterative structure refinement steps, though some NOEs remained ambiguous throughout the refinement process (Table 1).
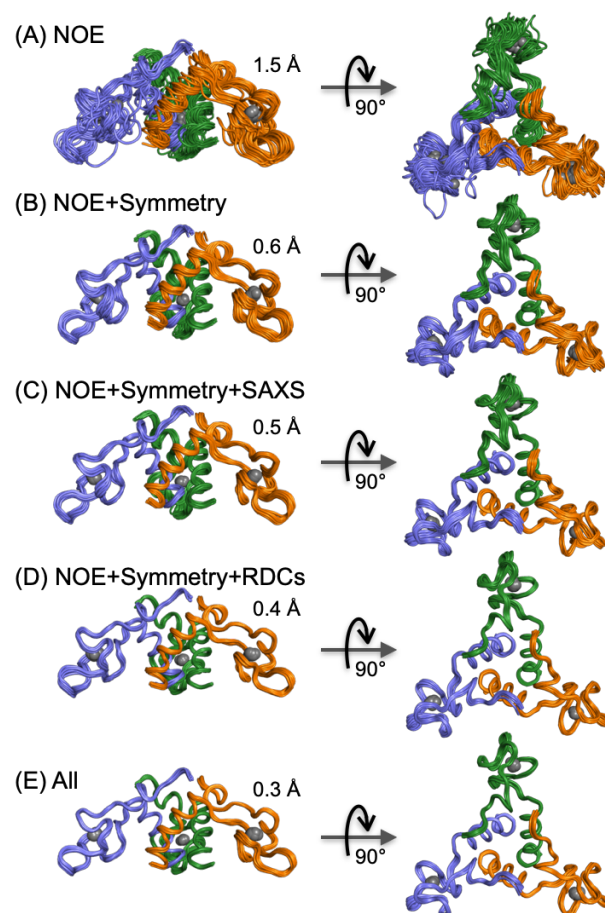

Figure 8. Impact of restraint classes on precision of AT_3 NMR ensemble. Each ensemble was computed using NMR-derived torsion angle restraints, and (A) NOEs, (B) NOEs and three-fold symmetry restraints, (C) NOEs, symmetry, special restraints from SAXS data, (D) NOEs, symmetry restraints and residual dipolar couplings, and (E) all restraint classes. Backbone RMSDs as indicated.

Symmetry, residual dipolar coupling (RDC) and SAXS restraints significantly increased the precision of the NMR structure (Figure 8). Ensembles computed using only NMR-derived distance and torsion angle restraints yielded poor convergence, with an overall backbone RMSD of 1.5 Å, and per-protomer backbone RMSD of 1.3 Å. RDCs and SAXS data improved the overall precision, but not as much as inclusion of three-fold symmetry restraints, which increased the overall precision by almost an Angstrom (from 1.5 Å to 0.6 Å).

Comparison to crystallographic and AlphaFold2 models

The final NMR ensemble was well defined by the restraints, with a backbone RMSD of 0.3 Å for C^α atoms (Figure 8, Figure 10, Table 1), and reveals a high degree of similarity with the trimers in the *B. subtilis* dodecamer (RMSD ~0.6 Å; Figure 10). This variance is similar to that observed between protomers in the experimentally determined crystal structure
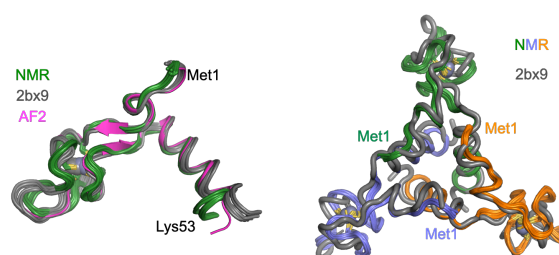

Figure 10. Solution structure of AT is congruent with its structure in AT_{12} and that predicted by AlphaFold2. Left, green, NMR ensemble of 20 conformers for chain A; grey, superposition of the twelve chains in the 2BX9 crystal structure; pink, AlphaFold2 prediction. Right, superposition of the AT_3 NMR derived ensemble with chains A-C (blue, orange, green) in the 2BX9 crystal structure.

(~0.6 Å for backbone atoms in 2BX9), and within the variance between those structures and that predicted by AlphaFold2 [49]. These subtle conformational differences imply intrinsic flexibility in the protein.

AT dynamics

Backbone amide ^{15}N R_1, R_2, and ^{1}H-^{15}N NOE relaxation rates were measured on both the 68 kDa dodecameric AT_{12} and 17 kDa trimeric AT_3 using conventional two-dimensional heteronuclear correlation spectra (Figure 9) [40,41]. Differences in the R_1 and R_2 relaxation rates for the two oligomeric states reflected the large difference in their rotational diffusion tensors; overall correlation times τ_m computed
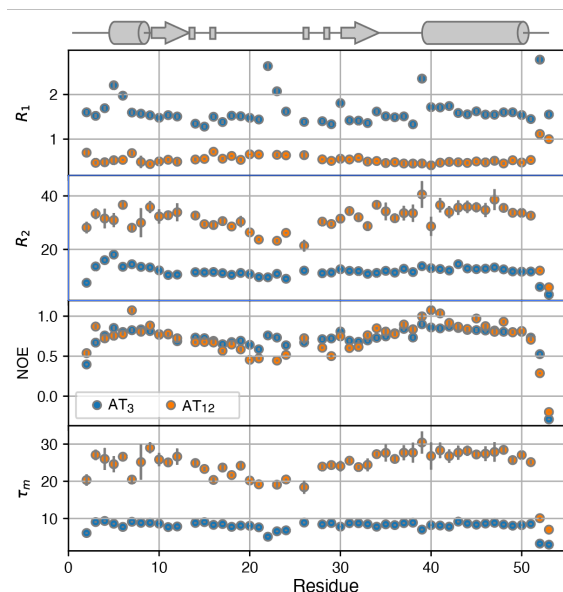

Figure 9. Amide ^{15}N relaxation rates for trimeric and dodecameric AT reveal differences in overall correlation and local dynamics. Relaxation rates were measured at 600 MHz, 55°C. Local correlation times were computed from the R_2/R_1 ratios {Palmer}. Secondary structures and location of metal ligands are indicated schematically above.

from the 10% trimmed mean R_2/R_1 ratios were 8 and 25 ns at 55 °C, respectively [50].

Hydrodynamic calculations based on the crystal structure of AT_{12}, and the R_2/R_1 ratios were also consistent with an isotropic diffusion tensor and an overall τ_m of 25 ns. However, R_2/R_1 ratios for AT_3 were consistent with an axially symmetric diffusion model with an anisotropic diffusion tensor, $D_{iso} = 2.00 \pm 0.01$ x 10^7 s^{-1}, $D_{\parallel/\perp} = 0.82 \pm 0.04$ ($\tau_m = 8.3$ ns).

Large differences in the rotational diffusion tensors of AT_{12} and AT_3 are accompanied with differences in internal motions. Amide ^{15}N relaxation rates were analyzed using the extended model-free formalism [51–53] to compare the amplitude internal dynamics of AT_3 and AT_{12} on the ps-ns timescale, as represented by the square of the generalized order parameter, S^2 (Figure 11). While both proteins exhibited generally high-order parameters, AT_3 and AT_{12} were found to exhibit local

Figure 11. Fitted Model-Free dynamics parameters suggest a stable helical bundle and flexible zinc-binding domains in AT_3, but less variable dynamics in AT_{12}. Top, fitted model free order parameters S^2 and R_{ex} for AT_3 and AT_{12}. Middle, fitted S^2 values mapped to the backbone of the AT trimer using a linear color ramp from the mean value (grey) to + (blue) or – (red) two standard deviations from the mean. Bottom, R_{ex} values mapped to the AT_3 structure with a color ramp from 0 to ≥ 4/s (yellow).

differences in fast internal motions. High S^2 values for AT_3 imply rigidity of the C-terminal helical bundle, and larger amplitude fast motions in the zinc binding arm domains and the N-terminal helix. By contrast, the zinc binding domains in AT_{12} are relatively rigid on the ps-ns time scales reported by S^2, likely a reflection of their packing onto adjacent zinc binding domains in the dodecamer (Figure 2). The two oligomeric forms of AT also exhibit different patterns of
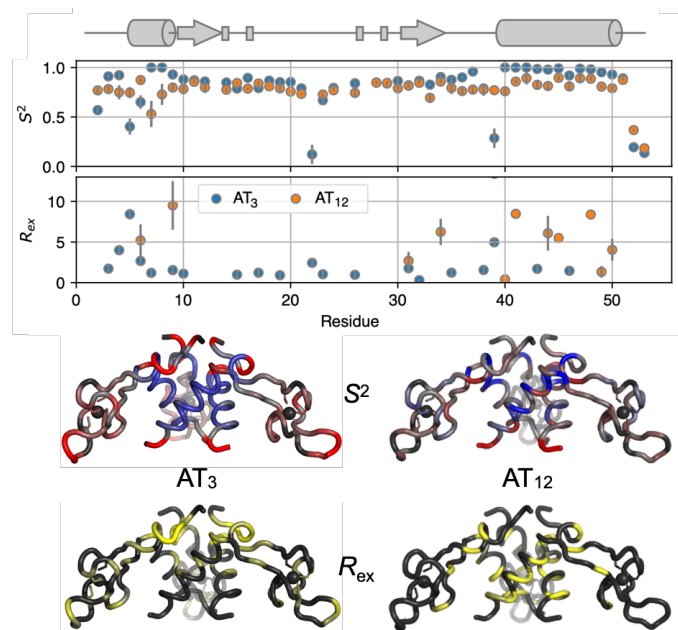
the phenomenological exchange broadening term R_{ex}, attributable to dynamics on slower µs-ms time scales [53,54]. For AT$_3$, the residues with largest R_{ex} terms are located at the N-terminus of the protomers, with smaller R_{ex} terms at the zinc binding domains. For AT$_{12}$, almost the inverse is observed, with the largest exchange terms needed to fit data for the helical bundle.

Discussion

Tryptophan biosynthesis is highly regulated in bacteria [18,55,56]. Within bacteria, TRAP-mediated transcription attenuation and translation repression via RNA binding represents an unusual regulatory mechanism. In the subset of organisms that also encode Anti-TRAP, its expression represents yet an additional regulatory layer by binding to and reversing the activity of an inhibitory protein. In this work we examined the equilibrium between active and inactive oligomeric states of *Bsu* Anti-TRAP using nMS, SAXS, AUC and NMR spectroscopy. We determined the solution structure of the active AT$_3$ form of the protein and observed differences in its internal dynamics relative to that of the inactive form AT$_{12}$. These studies thus help to inform our understanding of how AT inhibits RNA binding by Trp-bound TRAP, and of how the AT$_3 \leftrightarrow$ AT$_{12}$ equilibrium may provide yet another regulatory layer.

In our studies of *Bsu* AT, serendipity played a significant role. The fortuitous requirement of a mature amino-methionine terminus for stabilizing the AT dodecamer coincided with experimental zinc supplementation of minimal media for recombinant protein expression, which likely prevented maturation of a sizeable fraction of the protein. The second residue in *Bsu* AT is a valine, which is often a poor substrate of methionine aminopeptidase [57,58], thus ensuring retention of Met1 in the mature protein. The application of NMR and MS enabled detection of the formylated N-terminus, while denaturing reversed-phase chromatography allowed separation

of immature fAT from mature AT, which was not possible with conventional native purification. While the $AT_3 \leftrightarrow AT_{12}$ equilibrium is evident in samples of mature AT, the ability to prepare complexes of pure fAT provided an unambiguous means of establishing the role of the N-terminal amine in the equilibrium and enabling independent structural characterization of the TRAP-binding form of the protein (AT_3).

We found that $Bsu\ f$AT$_3$ (and AT_{12}) yields NMR spectra of exceptional quality, enabling complete resonance assignments and high-resolution structure determination by application of NMR, symmetry and SAXS restraints. Symmetry restraints were found to strongly increase the precision of the structural ensemble, while SAXS and RDC restraints provided modest improvements. We found the solution structure of AT_3 to be indistinguishable from that in the 12-mer crystal, or from the AF2 predicted model, indicating little conformational adjustment upon formation of the dodecamer.

While the average structure of the AT trimer in isolation and in the dodecamer are highly similar, they differ in their dynamics. Consistent with the overall size and shape of the oligomers, backbone ^{15}N relaxation measurements revealed an isotropic rotational diffusion tensor for AT_{12} and axially symmetric diffusion for the smaller AT_3. Model-free analysis of internal dynamics revealed flexible zinc ribbon motifs in AT_3, suggesting a role for the dynamics of these motifs in engaging Trp-bound TRAP rings. AT_{12} has comparatively more rigid zinc-binding domains, likely reflecting packing constraints from the other trimers in the tetrahedral arrangement. Modest R_{ex} terms in the N-terminal and zinc-binding domains of AT_3 may reflect transient but unproductive AT_3-AT_3 association reactions, whereas the pattern of R_{ex} terms is different in AT_{12}, perhaps reflecting transient dissociation to the AT_6 intermediate.

We conclude that the *Bsu* AT_3-AT_{12} equilibrium is dependent on the near-physiological pKa of the Met1 amine, with AT_{12} favored by a protonated N-terminus and AT_3 favored when unprotonated. Prior NMR observations [26] are corroborated here by nMS, SAXS, and AUC experiments as a function of pH. NMR spectra of *f*AT, over a pH range that alters the trimer-dodecamer equilibrium for mature AT, only show minor shift perturbations adjacent to His50, supporting the dominant role of the protonated N-terminus in stabilizing the dodecamer (Figure 7). Native MS spectra (at lower protein concentration) reveal AT_3 as the major species at pH 8, while at pH 6 nearly equal intensity is observed for ions arising from AT_3 and AT_{12} species (Figure 3); this provides some context to a prior nMS study which found exclusively AT_{12} when sprayed from pH-unadjusted ammonium acetate [25,34], which can approach a value of 4.75 in the ESI plume [59]. SAXS data for mature AT recorded as a function of pH and protein concentration could be well described by considering varying ratios of AT_3 and AT_{12} (Figure 5). Experimental curves could be reproduced form a linear combination of the form factors computed from the crystallographic dodecamer and a trimer extracted from the dodecamer. This finding is consistent with the failure to observe other assembly intermediates under equilibrium conditions. Sedimentation velocity (AUC) experiments further corroborate the pH-dependent equilibrium between AT_3 and AT_{12} and provide evidence for a short-lived AT_6 intermediate. If we consider AT_3 a "monomer" that can tetramerize, this behavior is consistent with biophysical characterization of other "tetramers", which predominantly follow a monomer-dimer-tetramer oligomerization path [60]. Small surface burial and minimal polar contacts in AT_6, result in transient/weak dimerization; large surface burial and many polar contacts favor AT_{12} upon collision of two AT_6 "dimers of trimers".

Conclusion

The mechanism by which Anti-TRAP (AT) promotes Trp production by inhibiting RNA binding by tryptophan-activated TRAP remains poorly understood [19,23,34,35]. The capacity of AT to form stable dodecameric and trimeric structures, wherein only the trimeric form is competent for binding and inhibiting TRAP is suggestive of a regulatory role for that equilibrium. While the complementary biophysical studies reported here provide qualitatively consistent insights into the properties of AT and its mechanism of oligomerization and TRAP inhibition, further work would be required to establish quantitative consistency. Some sources of uncertainty include the effect of molecular tumbling on observed NMR signal intensities, of ionizable buffers and of protein charge on gas phase ionization and gas phase signal detection, and relatively low structural resolution of SAXS and sedimentation velocity methods. Those caveats aside, it is clear that in vitro AT exhibits a slow equilibrium between active AT_3 and inactive AT_{12} states.

This slow association/dissociation behavior of AT could serve a regulatory function by kinetically modulating the response to changes in Trp concentration [61]. In this model (Figure 1), TRAP is slow to release Trp upon decrease in its cellular concentration and remains active for RNA binding and inhibiting *trp* expression. Meanwhile, decreasing cellular Trp results in accumulation of uncharged $tRNA^{Trp}$ and T-box mediated activation of AT expression. Expressed AT will trimerize and rapidly bind to RNA-free Trp-activated TRAP rings, preventing them from binding new *trp* RNA leaders. AT_3 that don't find TRAP rings could instead dodecamerize, resulting in slowly equilibrating populations of active AT_3 and inactive AT_{12}. This scenario would thus generate a pool of fast-acting AT_3 and a reservoir of slowly activated AT_{12}. The resulting steady-state equilibrium between AT_3, AT_{12}, AT_3-Trp-$TRAP_{11}$, Trp-$TRAP_{11}$ and Trp-$TRAP_{11}$-RNA would achieve a steady state of Trp homeostasis.

The properties of the AT$_3$ "triskelion", with its polydentate configuration of flexible zinc-binding arms, seem uniquely suited for capturing one or multiple TRAP rings, and thereby preventing RNA wrapping. The use of the amino terminus to mediate oligomerization represents a uniquely tuned equilibrium since the pKa and association constants are coupled, such that high protein concentration would shift the pKa to favor the protonated state, and thus the oligomer. It remains unclear why some species of Bacilli evolved to produce AT as an extra layer of regulation (e.g., *Bsu*, *Bli*), while others did not (e.g., *Bst, Bha*). This study highlights the lengths to which organisms have evolved sophisticated mechanisms for metabolic control, and the power of complementary biophysical measurements to describe those properties that enable regulated function.

Materials and Methods

Growth and purification of *B. subtilis* Anti-TRAP

AT was recombinantly expressed from *E. coli* from an engineered codon-optimized expression vector [26]. *B. subtilis* Anti-TRAP is a 53 amino acid polypeptide, with the sequence: MVIATDDLEV ACPKCERAGE IEGTPCPACS GKGVILTAQG YTLLDFIQKH LNK. It has a molecular weight of 5649.57 Da and its predicted extinction coefficient at 280 nm is 1490 M^{-1} cm^{-1} in its reduced form (Expasy ProtParam). Uniformly N-terminal formylmethionine Anti-TRAP (ƒAT) and deformylated AT were purified as previously described [26]. Briefly, transformed BL21(DE3) cells grown and induced in modified M9 minimal media were lysed and cellular debris pelleted by centrifugation. Isotope labeling was achieved by replacing unlabeled ammonium chloride with ^{15}N ammonium chloride for ^{15}N labeling, by substitution of ^{13}C glucose for ^{13}C/^{15}N double labeling. Heating of the cell lysate supernatant for 15 minutes at 70°C and

subsequent centrifugation removed most native *E. coli* proteins. The resulting supernatant was loaded onto Q-sepharose beads (GE healthcare) and eluted via a NaCl gradient. Eluted Anti-TRAP was denatured by addition of 6 M guanidinium and subjected to reverse-phase HPLC purification. AT (i.e., deformyl) and fAT elute at sufficiently resolved retention times from a C4 column to be separated and lyophilized, providing >99% desired species. Subsequent refolding results in intact fAT trimers for fAT, and $AT_3 + AT_{12}$ in equilibrium for (deformylated) AT.

Mass spectrometry

The theoretical mass of AT (from ExPASy ProtParam): Monomer (without Zn) = 5,649.57 Da; monomer with Zn (65.38 Da) = 5714.95 Da; trimer with three Zn = 17,144.85 Da; dodecamer with twelve Zn = 68,579.40 Da. AT samples were buffer exchanged twice into 100 mM ammonium acetate at 3 different pH's (pH 6.8, unadjusted; pH 8, adjusted using ammonium hydroxide; pH 6, adjusted using acetic acid) using size-exclusion spin columns (MicroBioSpin-6; Bio- Rad); the final concentration of AT was 10 μM. Borosilicate glass capillary emitters were pulled in-house with a Sutter Flaming/Brown Micropipette puller P97; samples were loaded and sprayed using nanoESI. Mass spectra were recorded on a Waters Synapt G2S mass spectrometer modified in-house with a SID device located between the trap cell and the drift cell. Data were recorded with capillary voltage, 0.7-1.0 kV; cone voltage, 20 V; extraction cone, 5-8 V; helium gas flow, 120 mL/min; trap gas flow, 2 mL/min; ion mobility nitrogen gas flow, 60 mL/min; source temperature 20 °C; trap wave velocity, 160 m/s; trap wave height, 4 V; ion mobility wave velocity, 300 m/s; ion mobility wave height, 20 V; transfer wave velocity, 65 m/s; transfer wave height, 2 V; time-of-flight analyzer pressure, $\sim 6\times10^{-7}$ mbar; and backing pressure, $\sim$ 2.5-3 mbar.

NMR assignments of AT$_{12}$

AT$_{12}$ predominates at high protein concentration, pH 7 for the mature, deformylated protein.

Two dimensional ^{1}H-^{15}N TROSY spectra of AT$_{12}$ have approximately the number of peaks

expected for the protomer, consistent with its molecular symmetry. HNCA, HNCOCA,

HNCACB, and HNCO triple resonance spectra recorded at 328 K using water flip-back solvent

suppression, sensitivity enhancement, and transverse relaxation optimized spectroscopy

(TROSY) coherence selection [62–66] on uniformly doubly labeled (^{13}C, ^{15}N) AT, allowed

assignment of every backbone resonance in the spectrum, corresponding to 48 of the 50 non-

proline residues (only M1 and E22 were missing).

NMR assignments and structural restraints of AT$_3$

*f*AT spectra exhibit signals exclusively attributable to trimeric AT. The NMR spectra of *f*AT3

also exhibit the number of peaks expected for the monomer, consistent with its molecular

symmetry. Assignments of uniformly, doubly labeled (^{13}C, ^{15}N) trimeric AT were obtained using

HNCO, HNCACB, CCONH-TOCSY, HCCONH-TOCSY, HCCH-COSY, HCCH-TOCSY, ^{15}N-

edited TOCSY, constant-time ^{13}C-edited HSQC, ^{13}C-edited HSQC, constant-time ^{13}C-edited

HSQC of the aromatic region, ^{13}C-edited HSQC of the aromatic region, and a ^{1}H-^{1}H plane and

^{1}H-^{13}C plane of the HCCH-COSY of the aromatic region [67].

Torsion angle restraints for the backbone φ angles were obtained from the analysis of 3D HNHA

spectra [68] and additional backbone torsion angle φ, ψ restraints were obtained from chemical

shifts using TALOS [69]. Sidechain χ$_1$ torsion angle restraints were obtained from the HNHB

and HACAHB-COSY experiments [68]. The X-Pro amide bonds for AT$_3$ were determined to be

in the trans conformation from analysis of the Cβ and Cγ chemical shifts [70]; Cγ shifts were not

assigned for AT_{12} but could be assigned as such in the crystal structure [28]. One bond $^1D_{HN-N}$ and $^1D_{N-C}$ residual dipolar coupling (RDC) restraints were obtained from IPAP spectra [71,72], of $^{13}C/^{15}N$-labeled AT aligned with 20 mg/ml Pf1 phage (ASLA Biotech). NOE restraints were obtained from a $^{13}C/^{15}N$-edited time-shared NOESY [73] in H_2O and a ^{13}C-edited NOESY [67] in ^2H_2O.

NOE assignments and initial AT_3 structure determination

NOE assignments of the symmetrical homo-trimer were made using the symmetry ambiguous distance restraint (symmetry ADR) method starting with a well-defined monomer [74,75]. The structure of the protomers were first obtained by assigning NOEs presumed to be intramolecular, (i.e., NOEs between zinc-coordinating coordinating cysteines, secondary structural elements inferred from secondary structure predictions based on sequence and chemical shift data), and using these as input for restrained torsion-angle refinement with CNS [76]. The set of 20 lowest energy structures (of 35 total) was then used with a 10 Å cutoff to filter through the remaining NOE data. At this stage, NOEs with less than six ambiguous assignments were used for another round of structure refinement and the cycle was iterated while decreasing the distance cutoff by 2 Å until the cutoff was 6 Å and the monomer structure converged to an RMSD of 2.08 Å for backbone atoms. The trimer structure was then calculated by ambiguously assigning any NOEs that could not be satisfied intramolecularly (i.e., they were defined as being between protomers A, B and C) and a structure calculation was performed utilizing non-crystallographic symmetry restraints in addition to the distance, orientation, and torsion angle restraints. This set of structures was then used with a 6 Å filter to assign the remaining NOEs and sort out the interprotomer contacts.

SAXS and RDC refinement of AT$_3$

To obtain a scattering profile for the trimer, pure fAT was purified, refolded and dialyzed against 50mM sodium-phosphate, pH 8, 100 mM NaCl, 200μM ZnCl$_2$ and 1mM TCEP. SAXS profiles at 1, 2, 3.3, 5, and 10mg/mL fAT (monomer) were acquired at the SIBYLS beamline at the Advanced Light Source in Berkeley, California. Data were obtained at a Q spacing range of 0.01 to 0.32 Å-1, and at 0.5, 1, and 6 second exposure times. The scattering contribution from the buffer was removed by subtracting the scattering profile of the dialysis solution. Processing, validation, and analysis of SAXS data was performed with the ATSAS package [77] and custom scripts. For restraints to the AT$_3$ structure, the 6 s exposure profile of the 3.3 mg/mL sample was used, as a small concentration-dependent amount of dodecamer (< 3% at 10 mg/mL) was detectable from deconvolution of the higher concentrations.

Isotropic and anisotropic IPAP spectra for RDC data were collected in 50 mM sodium-phosphate pH 6.6, 2mM DTT at 298 K in the absence and presence of 20 mg/mL $Pf1$ phage as the alignment medium. The lowest energy initial trimer structure (from above) was used as the starting point for simultaneous refinement against NOE, dihedral, RDC, and SAXS restraints in Xplor-NIH [78]. Agreement between measurements and values calculated from the structure was assessed using the DC server (https://spin.niddk.nih.gov/bax/nmrserver/dc/). Following refinement, the AT$_3$ structure ensemble was validated using protein structure validation server (PSVS) [79] and Procheck-NMR [80]. Final refinement and validation statistics are provided in Table 1.

NMR relaxation data

The ^{15}N relaxation data were recorded on a Bruker DRX 600 MHz spectrometer at 328 K using water flip-back and 3-9-19 WATERGATE solvent suppression, sensitivity improvement, and gradient coherence selection [67]. All relaxation data were recorded with a spectral width of 8389.26 Hz sampled over 1024 complex points in ω_2 (^1H) and a spectral width of 1763.75 Hz sampled over 64 complex points in ω_1 (^{15}N), with 16 scans per transient except for the NOE which was collected with 64 scans per transient, and with a recovery delay between transients of 3 seconds. The recovery delays for R_1 measurements were (100, 200, 400, 800, 1200, 1600, 2000, 2400 ms for AT_{12} and 10, 100, 250, 400, 550, 700, 850, 1250, and 2000 ms for AT_3); relaxation delays for R_2 measurements were (0, 9, 16.2, 23.4, 30.6, 37.8, 41.4, 45, 52.2, and 59.4 ms for AT_{12} and 0, 17, 33.9, 50.9, 67.8, 84.8, 101.8, 135.7, 169.6 ms for AT_3). The NOE values were determined as the ratio of the peak intensities from two interleaved spectra recorded with and without a 3 second ^1H presaturation period consisting of a series of 120º pulses separated by 5 ms delays. Relaxation rates were obtained by non-linear least-squares fitting measured peak heights with mono-exponential functions; uncertainties in peak heights were estimated from the standard deviation of the noise.

Rotational diffusion

Overall rotational correlation times, τ_m, and rotational diffusion tensors were determined experimentally from R_2/R_1 ratios [50] utilizing only R_2/R_1 ratios for residues with relaxation rates within one standard deviation of the 10% trimmed mean value. These calculations showed no statistical significance for fitting the NMR data to an axially symmetric or fully anisotropic diffusion tensor. Therefore, an isotropic diffusion tensor with a τ_m of 25 ns was used for the

model-free calculations of the dodecamer. This was supported by calculations of the hydrodynamic parameters by HYDRONMR [81,82] based on the dodecameric structure 2BX9 that also predict nearly isotropic tumbling for AT_{12}. The calculations based on the R_2/R_1 ratios of AT_3, however, indicated a statistically significant improvement for the axially symmetric model over the isotropic model. This was similarly supported by HYDRONMR calculations that yield an anisotropic diffusion tensor with two similar and one unique axis. Therefore, an axially symmetric diffusion tensor from the R_2/R_1 ratios was used for the model-free calculations of AT_3.

Model-free analysis

Model-free analysis for both AT_3 and AT_{12} [53] was performed using the program TENSOR v. 2 [83], which was recompiled to allow for input of up to 1000 residues and a CSA of -172 ppm [84]. Five motional models with up to three parameters describing the internal motions were used: (1) S^2 (2) S^2 and t_e (3) S^2 and R_{ex} (4) S^2, t_e, and R_{ex} (5) S^2, S^2_f, and t_e. Standard errors in the model-free parameters were obtained from Monte Carlo simulations using 1000 samples. Model fitting was performed using TENSOR v. 2 via a modified step-up hypothesis testing method [54].

Observation of the pH-dependent AT_3-AT_{12} equilibrium via SAXS

The program CRYSOL [45] was used to generate predicted scattering profiles AT_3 structure, the *B. subtilis* AT dodecamer retrieved from the RCSB (3BX9), and the *B. licheniformis* high-pH "inverted" dodecameric isoform (3LD0). Given the structural similarity of the AT trimer component between *B. subtilis* and *B. licheniformis* at nominal SAXS resolution (10-20 Å), the *B. licheniformis* dodecamer coordinates were used without modification. All three profiles were

normalized to the square of the input structure's molecular weight. The solvent density and contrast of the hydration shell were determined by fitting the scattering of the AT trimer structure against an empirical scattering profile of 5 mg/mL fAT in CRYSOL. The empirical scattering data from mature AT at 16 different pH and concentration conditions was fit with the program OLIGOMER [44], using the three predicted scattering profiles. An additional systematic term was also used to correct for baseline offset arising from incomplete buffer subtraction/mismatch.

Analytical ultracentrifugation

AT stock solutions were split and dialyzed against sample buffers at pH 7, 7.25, 7.5, and 8, consisting of 50 mM sodium phosphate, 100 mM NaCl, 0.5 mM tryptophan, and 0.02% (w/v) NaN_3. Sedimentation samples were subsequently made from the concentrated stock solutions with the corresponding dialysis buffer and allowed to equilibrate overnight. To account for the decreasing self-affinity at increasing pH, samples at pH 7-7.25 were made to 250, 125, and 65 µM AT monomer concentration, and at pH 7.5-8, to 500, 250, and 125 µM. Dilutions were performed on a gravimetric balance accurate to 0.2 mg, with an assumed solution density of 1.0 g/ml. Sedimentation velocity data were obtained at 25 °C using a Beckman Coulter ProteomeLab XL-I ultracentrifuge equipped with an 8-position rotor and double-sector cells with sapphire windows. Matched dialysis buffer was present in the reference sector. Data were recorded using interference optics with a scan interval of one minute and 200 scans per cell at a rotor speed of 50,000 rpm. The position of the meniscus and cell bottom were determined for each cell by fitting a sedimentation coefficient distribution and uniform frictional value f/f$_0$ in SEDFIT [85] at a sampling interval of 10 to 20 points per Svedberg. Time and radial invariant noise were

removed from each interference scan. The buffer density ρ and viscosity η under these conditions were calculated by SEDNTRP [86] to be 1.01260 g/mol and 1.0520 cP, respectively.

Determination of kinetic parameters for the $AT_3 \leftrightarrow AT_6 \leftrightarrow AT_{12}$ model in SEDPHAT [43] was performed by globally fitting 200 interference scans from each set of AT concentrations at one pH (600 scans total). In addition to model kinetic parameters, the fringe shift coefficient, apparent sedimentation coefficients for AT_3, AT_6, and AT_{12}, as well as the molar mass for the trimer were also optimized. pH 8 data were fit first, using the HYDROPRO [87]-predicted sedimentation coefficients of 2.1 S and 4.1 S at 25 °C for AT_3 and AT_{12}, respectively, as starting sedimentation coefficients. The AT_6 starting sedimentation coefficient was set to 3 S. Initial parameters were 10^5 M^{-1} for k_1, 10^{-3} s^{-1} for k_{-1}, 10^6 M^{-1} for k_2, and 10^{-4} s^{-1} for k_{-2}, as these provided reasonable predicted interference curves. The apparent molar weight of AT in the experiment was also optimized, using the expected mass of the trimer as a starting value. A reasonable starting point for the molar absorptivity was determined by manual iterative evaluations of the model using different values until a fringe shift of appropriate magnitude was achieved. (Uncertainty analysis in the kinetic parameters was attempted through Monte-Carlo estimation of errors, but after 1000 evaluations no variance in the fitted parameters was detected.)

Interfaces

Solvent accessible surface (SAS) area burial between protomers was computed using PyMOL 2.5.2 (Schrödinger, LLC) using a dot density of 3. Burial was computed from difference between the SAS of components and their complex, using PyMOL get_area. SAS burial for folding of the

protomer was estimated from multiple conformations using PROSA [88]. Similar interface and surface areas were obtained using PISA [89]

Acknowledgements

Table 1: NMR structural statistics for AT ensemble (20 structures):

NOE-based distance constraints:			
Total ambiguous (not included in statistics)	528		
Total unambiguous	3396		
Inter-protomer	396		
Intra-residue [i = j]	611		
Sequential [| i - j | = 1]	1007		
Medium range [1 < | i - j | < 5]	891		
Long range [| i - j | > 5]	887		
NOE constraints per restrained residue	64.1		
Torsion-angle constraints:	318		
Total number of restricting constraints	3714		
Total number of restricting constraints per restrained residue	70.1		
Restricting long-range constraints per restrained residue	16.7		
Number of structures used	20		
Residual constraint violations			
Distance violations / structure > 0.5 Å	1		
RMS of distance violation / constraint	0.03 Å		
Dihedral angle violations / structure > 10 °	11.3		
RMS of dihedral angle violation / constraint	3.42 °		
RMSD Values			
Backbone atoms (all residues)	0.4 Å		
Heavy atoms (all residues)	0.6 Å		
Structure Quality Factors - overall statistics	Mean	SD	Z-score
Procheck G-factor (phi/psi only)	-0.79	n/a	-2.79
Procheck G-factor (all dihedral angles)	-0.67	n/a	3.96
Verify3D	0.09	0.0065	-5.94
ProsaII (-ve)	0.40	0.0265	-1.03
MolProbity clash score	196.35	8.4019	-32.17
Ramachandran Statistics			
Most favored	74.0%		
Additionally allowed	24.2%		
Generously allowed	1.8%		
Disallowed regions	0.0%		

Summary of conformationally-restricting constraints and structure quality factors from protein structure and validation server (PSVS).

References

[1]   P. Babitzke, J.T. Stults, S.J. Shire, C. Yanofsky, TRAP, the trp RNA-binding attenuation protein of Bacillus subtilis, is a multisubunit complex that appears to recognize G/UAG repeats in the trpEDCFBA and trpG transcripts, J. Biol. Chem. 269 (1994) 16597–16604.

[2]   P. Babitzke, C. Yanofsky, Reconstitution of Bacillus subtilis trp attenuation in vitro with TRAP, the trp RNA-binding attenuation protein, Proc. Natl. Acad. Sci. U. S. A. 90 (1993) 133–137.

[3]   P. Gollnick, Regulation of the Bacillus subtilis trp operon by an RNA-binding protein, Mol. Microbiol. 11 (1994) 991–997.

[4]   P. Gollnick, S. Ishino, M.I. Kuroda, D.J. Henner, C. Yanofsky, The mtr locus is a two-gene operon required for transcription attenuation in the trp operon of Bacillus subtilis, Proc. Natl. Acad. Sci. U. S. A. 87 (1990) 8726–8730. https://doi.org/10.1073/pnas.87.22.8726.

[5]   E. Merino, P. Babitzke, C. Yanofsky, trp RNA-binding attenuation protein (TRAP)-trp leader RNA interactions mediate translational as well as transcriptional regulation of the Bacillus subtilis trp operon, J. Bacteriol. 177 (1995) 6362–6370.

[6]   J.P. Sarsero, E. Merino, C. Yanofsky, A Bacillus subtilis operon containing genes of unknown function senses tRNATrp charging and regulates expression of the genes of tryptophan biosynthesis, Proc Natl Acad Sci U A. 97 (2000) 2656–61.

[7]   M. Yang, A. de Saizieu, A.P. van Loon, P. Gollnick, Translation of trpG in Bacillus subtilis is regulated by the trp RNA- binding attenuation protein (TRAP), J Bacteriol. 177 (1995) 4272–8.

[8]   H. Yakhnin, J.E. Babiarz, A.V. Yakhnin, P. Babitzke, Expression of the Bacillus subtilis trpEDCFBA Operon Is Influenced by Translational Coupling and Rho Termination Factor, J. Bacteriol. 183 (2001) 5918–5926. https://doi.org/10.1128/JB.183.20.5918-5926.2001.

[9]   H. Du, P. Babitzke, trp RNA-binding attenuation protein-mediated long distance RNA refolding regulates translation of trpE in Bacillus subtilis, J. Biol. Chem. 273 (1998) 20494–20503.

[10]   H. Yakhnin, H. Zhang, A.V. Yakhnin, P. Babitzke, The trp RNA-binding attenuation protein of Bacillus subtilis regulates translation of the tryptophan transport gene trpP (yhaG) by blocking ribosome binding, J. Bacteriol. 186 (2004) 278–286. https://doi.org/10.1128/JB.186.2.278-286.2004.

[11]   D.J. Henner, L. Band, H. Shimotsu, Nucleotide sequence of the Bacillus subtilis tryptophan operon, Gene. 34 (1985) 169–77.

[12] K.D. Potter, N.M. Merlino, T. Jacobs, P. Gollnick, TRAP binding to the Bacillus subtilis trp leader region RNA causes efficient transcription termination at a weak intrinsic terminator, Nucleic Acids Res. 39 (2011) 2092–2102. https://doi.org/10.1093/nar/gkq965.

[13] N.M. McAdams, P. Gollnick, The Bacillus subtilis TRAP Protein Can Induce Transcription Termination in the Leader Region of the Tryptophan Biosynthetic (trp) Operon Independent of the trp Attenuator RNA, PLoS ONE. 9 (2014) e88097. https://doi.org/10.1371/journal.pone.0088097.

[14] J.E. Schaak, H. Yakhnin, P.C. Bevilacqua, P. Babitzke, A Mg2+-dependent RNA tertiary structure forms in the Bacillus subtilis trp operon leader transcript and appears to interfere with trpE translation control by inhibiting TRAP binding, J. Mol. Biol. 332 (2003) 555–574.

[15] A.I. Lee, J.P. Sarsero, C. Yanofsky, A temperature-sensitive trpS mutation interferes with trp RNA-binding attenuation protein (TRAP) regulation of trp gene expression in Bacillus subtilis, J. Bacteriol. 178 (1996) 6518–6524. https://doi.org/10.1128/jb.178.22.6518-6524.1996.

[16] H. Du, R. Tarpey, P. Babitzke, The trp RNA-binding attenuation protein regulates TrpG synthesis by binding to the trpG ribosome binding site of Bacillus subtilis, J. Bacteriol. 179 (1997) 2582–2586. https://doi.org/10.1128/jb.179.8.2582-2586.1997.

[17] A. Gutiérrez-Preciado, T.M. Henkin, F.J. Grundy, C. Yanofsky, E. Merino, Biochemical features and functional implications of the RNA-based T-box regulatory mechanism, Microbiol. Mol. Biol. Rev. MMBR. 73 (2009) 36–61. https://doi.org/10.1128/MMBR.00026-08.

[18] A. Gutiérrez-Preciado, C. Yanofsky, E. Merino, Comparison of tryptophan biosynthetic operon regulation in different Gram-positive bacterial species, Trends Genet. 23 (2007) 422–427. https://doi.org/10.1016/j.tig.2007.05.005.

[19] A. Valbuzzi, C. Yanofsky, Inhibition of the B. subtilis regulatory protein TRAP by the TRAP- inhibitory protein, AT, Science. 293 (2001) 2057–9.

[20] S. Sharma, P. Gollnick, Modulating TRAP-mediated transcription termination by AT during transcription of the leader region of the Bacillus subtilis trp operon, Nucleic Acids Res. 42 (2014) 5543–5555. https://doi.org/10.1093/nar/gku211.

[21] G. Chen, C. Yanofsky, Tandem transcription and translation regulatory sensing of uncharged tryptophan tRNA, Science. 301 (2003) 211–3.

[22] G. Chen, C. Yanofsky, Features of a leader peptide coding region that regulate translation initiation for the anti-TRAP protein of B. subtilis, Mol. Cell. 13 (2004) 703–711. https://doi.org/10.1016/s1097-2765(04)00085-1.

[23] D. Snyder, J. Lary, Y. Chen, P. Gollnick, J.L. Cole, Interaction of the trp RNA-binding Attenuation Protein (TRAP) with Anti-TRAP, J. Mol. Biol. 338 (2004) 669–682. https://doi.org/10.1016/j.jmb.2004.03.030.

[24] A. Valbuzzi, C. Yanofsky, Zinc is required for assembly and function of the anti-trp RNA-binding attenuation protein, AT, J. Biol. Chem. 277 (2002) 48574–48578. https://doi.org/10.1074/jbc.M208980200.

[25] S. Akashi, M. Watanabe, J.G. Heddle, S. Unzai, S.-Y. Park, J.R.H. Tame, RNA and Protein Complexes of trp RNA-Binding Attenuation Protein Characterized by Mass Spectrometry, Anal. Chem. 81 (2009) 2218–2226. https://doi.org/10.1021/ac802354j.

[26] J.R. Sachleben, C.A. McElroy, P. Gollnick, M.P. Foster, Mechanism for pH-dependent gene regulation by amino-terminus-mediated homooligomerization of Bacillus subtilis anti-trp RNA-binding attenuation protein, Proc. Natl. Acad. Sci. U. S. A. 107 (2010) 15385–15390. https://doi.org/10.1073/pnas.1004981107.

[27] M.B. Shevtsov, Y. Chen, P. Gollnick, A.A. Antson, Anti-TRAP protein from Bacillus subtilis: crystallization and internal symmetry, Acta Crystallogr Biol Crystallogr. 60 (2004) 1311–4.

[28] M.B. Shevtsov, Y. Chen, P. Gollnick, A.A. Antson, Crystal structure of Bacillus subtilis anti-TRAP protein, an antagonist of TRAP/RNA interaction, Proc. Natl. Acad. Sci. U. S. A. 102 (2005) 17600–17605. https://doi.org/10.1073/pnas.0508728102.

[29] M.B. Shevtsov, Y. Chen, M.N. Isupov, A. Leech, P. Gollnick, A.A. Antson, Bacillus licheniformis Anti-TRAP can assemble into two types of dodecameric particles with the same symmetry but inverted orientation of trimers, J. Struct. Biol. 170 (2010) 127–133. https://doi.org/10.1016/j.jsb.2010.01.013.

[30] T.J. Sereda, C.T. Mant, A.M. Quinn, R.S. Hodges, Effect of the α-amino group on peptide retention behaviour in reversed-phase chromatography Determination of the pKa values of the α-amino group of 19 different N-terminal amino acid residues, J. Chromatogr. A. 646 (1993) 17–30. https://doi.org/10.1016/S0021-9673(99)87003-4.

[31] M.G. McCammon, H. Hernández, F. Sobott, C.V. Robinson, Tandem Mass Spectrometry Defines the Stoichiometry and Quaternary Structural Arrangement of Tryptophan Molecules in the Multiprotein Complex TRAP, J. Am. Chem. Soc. 126 (2004) 5950–5951. https://doi.org/10.1021/ja0317170.

[32] O.W. Bayfield, C.-S. Chen, A.R. Patterson, W. Luan, C. Smits, P. Gollnick, A.A. Antson, Trp RNA-Binding Attenuation Protein: Modifying Symmetry and Stability of a Circular Oligomer, PLoS ONE. 7 (2012) e44309. https://doi.org/10.1371/journal.pone.0044309.

[33] C.-S. Chen, C. Smits, G.G. Dodson, M.B. Shevtsov, N. Merlino, P. Gollnick, A.A. Antson, How to Change the Oligomeric State of a Circular Protein Assembly: Switch from 11-Subunit to 12-Subunit TRAP Suggests a General Mechanism, PLOS ONE. 6 (2011) e25296. https://doi.org/10.1371/journal.pone.0025296.

[34] M. Watanabe, J.G. Heddle, K. Kikuchi, S. Unzai, S. Akashi, S.-Y. Park, J.R.H. Tame, The nature of the TRAP-Anti-TRAP complex, Proc. Natl. Acad. Sci. U. S. A. 106 (2009) 2176–2181. https://doi.org/10.1073/pnas.0801032106.

[35] E.C. Ihms, M. Zhou, Y. Zhang, I.R. Kleckner, C.A. McElroy, V.H. Wysocki, P. Gollnick, M.P. Foster, Gene regulation by substoichiometric heterocomplex formation of undecameric TRAP and trimeric anti-TRAP, Proc. Natl. Acad. Sci. 111 (2014) 3442–3447. https://doi.org/10.1073/pnas.1315281111.

[36] R. Jain, B. Hao, R. Liu, M.K. Chan, Structures of E. coli Peptide Deformylase Bound to Formate: Insight into the Preference for Fe2+ over Zn2+ as the Active Site Metal, J. Am. Chem. Soc. 127 (2005) 4558–4559. https://doi.org/10.1021/ja0503074.

[37] S. Ragusa, S. Blanquet, T. Meinnel, Control of peptide deformylase activity by metal cations 11Edited by A. R. Fersht, J. Mol. Biol. 280 (1998) 515–523. https://doi.org/10.1006/jmbi.1998.1883.

[38] C.A. McElroy, Dynamics and function: mechanistic studies of the gene regulatory proteins TRAP and anti-TRAP, The Ohio State University, 2005. https://etd.ohiolink.edu/apexprod/rws_olink/r/1501/10?clear=10&p10_accession_num=osu1111429539 (accessed June 27, 2023).

[39] L.E. Kay, D.A. Torchia, A. Bax, Backbone dynamics of proteins as studied by 15N inverse detected heteronuclear NMR spectroscopy: application to staphylococcal nuclease, Biochemistry. 28 (1989) 8972–9.

[40] G. Barbato, M. Ikura, L.E. Kay, R.W. Pastor, A. Bax, Backbone dynamics of calmodulin studied by 15N relaxation using inverse detected two-dimensional NMR spectroscopy: the central helix is flexible, Biochemistry. 31 (1992) 5269–5278.

[41] N.A. Farrow, R. Muhandiram, A.U. Singer, S.M. Pascal, C.M. Kay, G. Gish, S.E. Shoelson, T. Pawson, J.D. Forman-Kay, L.E. Kay, Backbone dynamics of a free and phosphopeptide-complexed Src homology 2 domain studied by 15N NMR relaxation, Biochemistry. 33 (1994) 5984–6003. https://doi.org/10.1021/bi00185a040.

[42] C.A. Brautigam, Using Lamm-Equation modeling of sedimentation velocity data to determine the kinetic and thermodynamic properties of macromolecular interactions, Methods. 54 (2011) 4–15. https://doi.org/10.1016/j.ymeth.2010.12.029.

[43] H. Zhao, G. Piszczek, P. Schuck, SEDPHAT – A platform for global ITC analysis and global multi-method analysis of molecular interactions, Methods. 76 (2015) 137–148. https://doi.org/10.1016/j.ymeth.2014.11.012.

[44] P.V. Konarev, V.V. Volkov, A.V. Sokolova, M.H.J. Koch, D.I. Svergun, PRIMUS: a Windows PC-based system for small-angle scattering data analysis, J. Appl. Crystallogr. 36 (2003) 1277–1282. https://doi.org/10.1107/S0021889803012779.

[45] D. Svergun, C. Barberato, M.H.J. Koch, CRYSOL – a Program to Evaluate X-ray Solution Scattering of Biological Macromolecules from Atomic Coordinates, J. Appl. Crystallogr. 28 (1995) 768–773. https://doi.org/10.1107/S0021889895007047.

[46] C. McElroy, A. Manfredo, A. Wendt, P. Gollnick, M. Foster, TROSY-NMR Studies of the 91kDa TRAP Protein Reveal Allosteric Control of a Gene Regulatory Protein by Ligand-altered Flexibility, J. Mol. Biol. 323 (2002) 463–473. https://doi.org/10.1016/S0022-2836(02)00940-3.

[47] I.R. Kleckner, P. Gollnick, M.P. Foster, Mechanisms of allosteric gene regulation by NMR quantification of microsecond-millisecond protein dynamics, J. Mol. Biol. 415 (2012) 372–381. https://doi.org/10.1016/j.jmb.2011.11.019.

[48] S.E. Boyken, M.A. Benhaim, F. Busch, M. Jia, M.J. Bick, H. Choi, J.C. Klima, Z. Chen, C. Walkey, A. Mileant, A. Sahasrabuddhe, K.Y. Wei, E.A. Hodge, S. Byron, A. Quijano-Rubio, B. Sankaran, N.P. King, J. Lippincott-Schwartz, V.H. Wysocki, K.K. Lee, D. Baker, De novo design of tunable, pH-driven conformational changes, Science. 364 (2019) 658–664. https://doi.org/10.1126/science.aav7897.

[49] J. Jumper, R. Evans, A. Pritzel, T. Green, M. Figurnov, O. Ronneberger, K. Tunyasuvunakool, R. Bates, A. Žídek, A. Potapenko, A. Bridgland, C. Meyer, S.A.A. Kohl, A.J. Ballard, A. Cowie, B. Romera-Paredes, S. Nikolov, R. Jain, J. Adler, T. Back, S. Petersen, D. Reiman, E. Clancy, M. Zielinski, M. Steinegger, M. Pacholska, T. Berghammer, S. Bodenstein, D. Silver, O. Vinyals, A.W. Senior, K. Kavukcuoglu, P. Kohli, D. Hassabis, Highly accurate protein structure prediction with AlphaFold, Nature. 596 (2021) 583–589. https://doi.org/10.1038/s41586-021-03819-2.

[50] L.K. Lee, M. Rance, W.J. Chazin, A.G. Palmer, Rotational diffusion anisotropy of proteins from simultaneous analysis of 15N and 13C alpha nuclear spin relaxation, J. Biomol. NMR. 9 (1997) 287–298. https://doi.org/10.1023/a:1018631009583.

[51] G. Lipari, A. Szabo, A Model-free approach to the interpretation of nuclear magnetic resonance relaxation in macromolecules. 1. theory and range of validity, J Am Chem Soc. 104 (1982) 4546–4559.

[52] G. Lipari, A. Szabo, A model-free approach to the interpretation of nuclear magnetic resonance relaxation in macromolecules. 2. Analysis of experimental results, J Am Chem Soc. 104 (1982) 4559–4570.

[53] G.M. Clore, A. Szabo, A. Bax, L.E. Kay, P.C. Driscoll, A.M. Gronenborn, Deviations from the simple two-parameter model-free approach to the interpretation of nitrogen-15 nuclear magnetic relaxation of proteins, J. Am. Chem. Soc. 112 (1990) 4989–4991. https://doi.org/10.1021/ja00168a070.

[54] A.M. Mandel, M. Akke, A.G. Palmer 3rd, Backbone dynamics of Escherichia coli ribonuclease HI: correlations with structure and function in an active enzyme, J Mol Biol. 246 (1995) 144–63.

[55] C. Yanofsky, RNA-based regulation of genes of tryptophan synthesis and degradation, in bacteria, RNA. 13 (2007) 1141–1154. https://doi.org/10.1261/rna.620507.

[56] E. Merino, R.A. Jensen, C. Yanofsky, Evolution of bacterial trp operons and their regulation, Curr. Opin. Microbiol. 11 (2008) 78–86. https://doi.org/10.1016/j.mib.2008.02.005.

[57] P.H. Hirel, M.J. Schmitter, P. Dessen, G. Fayat, S. Blanquet, Extent of N-terminal methionine excision from Escherichia coli proteins is governed by the side-chain length of the penultimate amino acid., Proc. Natl. Acad. Sci. 86 (1989) 8247–8251. https://doi.org/10.1073/pnas.86.21.8247.

[58] F. Frottin, A. Martinez, P. Peynot, S. Mitra, R.C. Holz, C. Giglione, T. Meinnel, The proteomics of N-terminal methionine cleavage, Mol. Cell. Proteomics MCP. 5 (2006) 2336–2349. https://doi.org/10.1074/mcp.M600225-MCP200.

[59] L. Konermann, Addressing a Common Misconception: Ammonium Acetate as Neutral pH "Buffer" for Native Electrospray Mass Spectrometry, J. Am. Soc. Mass Spectrom. 28 (2017) 1827–1835. https://doi.org/10.1007/s13361-017-1739-3.

[60] E.T. Powers, D.L. Powers, A Perspective on Mechanisms of Protein Tetramer Formation, Biophys. J. 85 (2003) 3587–3599. https://doi.org/10.1016/S0006-3495(03)74777-8.

[61] C. Frieden, Protein oligomerization as a metabolic control mechanism: Application to apoE, Protein Sci. 28 (2019) 837–842. https://doi.org/10.1002/pro.3583.

[62] K. Pervushin, R. Riek, G. Wider, K. Wüthrich, Attenuated T2 relaxation by mutual cancellation of dipole–dipole coupling and chemical shift anisotropy indicates an avenue to NMR structures of very large biological macromolecules in solution, Proc. Natl. Acad. Sci. 94 (1997) 12366–12371.

[63] J.P. Loria, M. Rance, A.G. Palmer, Transverse-relaxation-optimized (TROSY) gradient-enhanced triple-resonance NMR spectroscopy, J. Magn. Reson. San Diego Calif 1997. 141 (1999) 180–184. https://doi.org/10.1006/jmre.1999.1891.

[64] M. Rance, J.P. Loria, null Palmer AG3rd, Sensitivity improvement of transverse relaxation-optimized spectroscopy, J. Magn. Reson. San Diego Calif 1997. 136 (1999) 92–101. https://doi.org/10.1006/jmre.1998.1626.

[65] M. Salzmann, K. Pervushin, G. Wider, H. Senn, K. Wuthrich, TROSY in triple-resonance experiments: new perspectives for sequential NMR assignment of large proteins, Proc Natl Acad Sci U A. 95 (1998) 13585–90.

[66] M. Salzmann, G. Wider, K. Pervushin, K. Wuthrich, Improved sensitivity and coherence selection for [15N,1H]-TROSY elements in triple resonance experiments, J Biomol NMR. 15 (1999) 181–4.

[67] J. Cavanagh, W.J. Fairbrother, A.G.P. Iii, N.J. Skelton, M. Rance, Protein NMR Spectroscopy, Second Edition: Principles and Practice, Academic Press, 2006. http://www.amazon.com/Protein-NMR-Spectroscopy-Second-Edition/dp/012164491X.

[68] A. Bax, G.W. Vuister, S. Grzesiek, F. Delaglio, A.C. Wang, R. Tschudin, G. Zhu, Measurement of homo- and heteronuclear J couplings from quantitative J correlation, Methods Enzym. 239 (1994) 79–105.

[69] G. Cornilescu, F. Delaglio, A. Bax, Protein backbone angle restraints from searching a database for chemical shift and sequence homology, J Biomol NMR. 13 (1999) 289–302.

[70] M. Schubert, D. Labudde, H. Oschkinat, P. Schmieder, A software tool for the prediction of Xaa-Pro peptide bond conformations in proteins based on 13C chemical shift statistics, J. Biomol. NMR. 24 (2002) 149–154. https://doi.org/10.1023/a:1020997118364.

[71] M. Ottiger, F. Delaglio, A. Bax, Measurement of J and dipolar couplings from simplified two-dimensional NMR spectra, J Magn Reson. 131 (1998) 373–8.

[72] P. Permi, Measurement of residual dipolar couplings from 1Halpha to 13Calpha and 15N using a simple HNCA-based experiment, J Biomol NMR. 27 (2003) 341–9.

[73] M. Sattler, M. Maurer, J. Schleucher, C. Griesinger, A simultaneous (15)N, (1)H- and (13)C, (1)H-HSQC with sensitivity enhancement and a heteronuclear gradient echo, J. Biomol. NMR. 5 (1995) 97–102. https://doi.org/10.1007/BF00227475.

[74] H. Kovacs, S.I. O'Ddonoghue, H.-J. Hoppe, D. Comfort, K.B.M. Reid, lain D. Campbell, M. Nilges, Solution structure of the coiled-coil trimerization domain from lung surfactant protein D, J. Biomol. NMR. 24 (2002) 89–102. https://doi.org/10.1023/a:1020980006628.

[75] S.I. O'Donoghue, X. Chang, R. Abseher, M. Nilges, J.J. Led, Unraveling the symmetry ambiguity in a hexamer: calculation of the R6 human insulin structure, J Biomol NMR. 16 (2000) 93–108.

[76] A.T. Brunger, Version 1.2 of the Crystallography and NMR system, Nat. Protoc. 2 (2007) 2728–2733. https://doi.org/10.1038/nprot.2007.406.

[77] K. Manalastas-Cantos, P.V. Konarev, N.R. Hajizadeh, A.G. Kikhney, M.V. Petoukhov, D.S. Molodenskiy, A. Panjkovich, H.D.T. Mertens, A. Gruzinov, C. Borges, C.M. Jeffries, D.I. Svergun, D. Franke, ATSAS 3.0: expanded functionality and new tools for small-angle scattering data analysis, J. Appl. Crystallogr. 54 (2021) 343–355. https://doi.org/10.1107/S1600576720013412.

[78] C.D. Schwieters, G.A. Bermejo, G.M. Clore, Xplor-NIH for molecular structure determination from NMR and other data sources, Protein Sci. 27 (2018) 26–40. https://doi.org/10.1002/pro.3248.

[79] A. Bhattacharya, R. Tejero, G.T. Montelione, Evaluating protein structures determined by structural genomics consortia, Proteins Struct. Funct. Bioinforma. 66 (2007) 778–795. https://doi.org/10.1002/prot.21165.

[80] R.A. Laskowski, J.A. Rullmannn, M.W. MacArthur, R. Kaptein, J.M. Thornton, AQUA and PROCHECK-NMR: programs for checking the quality of protein structures solved by NMR, J. Biomol. NMR. 8 (1996) 477–486. https://doi.org/10.1007/BF00228148.

[81] J. García de la Torre, M.L. Huertas, B. Carrasco, HYDRONMR: prediction of NMR relaxation of globular proteins from atomic-level structures and hydrodynamic calculations, J. Magn. Reson. San Diego Calif 1997. 147 (2000) 138–146. https://doi.org/10.1006/jmre.2000.2170.

[82] P. Bernadó, J. García de la Torre, M. Pons, Interpretation of 15N NMR relaxation data of globular proteins using hydrodynamic calculations with HYDRONMR, J. Biomol. NMR. 23 (2002) 139–150. https://doi.org/10.1023/a:1016359412284.

[83] P. Dosset, J.C. Hus, M. Blackledge, D. Marion, Efficient analysis of macromolecular rotational diffusion from heteronuclear relaxation data, J. Biomol. NMR. 16 (2000) 23–28. https://doi.org/10.1023/a:1008305808620.

[84] A.L. Lee, A.J. Wand, Assessing potential bias in the determination of rotational correlation times of proteins by NMR relaxation, J. Biomol. NMR. 13 (1999) 101–112. https://doi.org/10.1023/a:1008304220445.

[85] P. Schuck, Analytical Ultracentrifugation as a Tool for Studying Protein Interactions, Biophys. Rev. 5 (2013) 159–171. https://doi.org/10.1007/s12551-013-0106-2.

[86] J.S. Philo, SEDNTERP: a calculation and database utility to aid interpretation of analytical ultracentrifugation and light scattering data, Eur. Biophys. J. EBJ. (2023). https://doi.org/10.1007/s00249-023-01629-0.

[87] J. García De La Torre, M.L. Huertas, B. Carrasco, Calculation of hydrodynamic properties of globular proteins from their atomic-level structure, Biophys. J. 78 (2000) 719–730. https://doi.org/10.1016/S0006-3495(00)76630-6.

[88] J. Estrada, P. Bernadó, M. Blackledge, J. Sancho, ProtSA: a web application for calculating sequence specific protein solvent accessibilities in the unfolded ensemble, BMC Bioinformatics. 10 (2009) 104. https://doi.org/10.1186/1471-2105-10-104.

[89] E. Krissinel, K. Henrick, Inference of Macromolecular Assemblies from Crystalline State, J. Mol. Biol. 372 (2007) 774–797. https://doi.org/10.1016/j.jmb.2007.05.022.